Chiral magnetism in lithium-decorated monolayer $CrTe_2$: Interplay between Dzyaloshinskii-Moriya interaction and higher-order interactions

Weiyi Pan,[1] Changsong Xu,[2,3,*] Xueyang Li,[2,3] Zhiming Xu,[1] Boyu Liu,[2,3] Bing-Lin Gu,[1,4] and Wenhui Duan[1,4,5]

[1]*State Key Laboratory of Low Dimensional Quantum Physics and Department of Physics, Tsinghua University, Beijing 100084, China*

[2]*Key Laboratory of Computational Physical Science (Ministry of Education), State Key Laboratory of Computational Physical Science, and Department of Physics, Fudan University, Shanghai 200433, China*

[3]*Shanghai Qi Zhi Institute, Shanghai 200030, China*

[4]*Institute for Advanced Study, Tsinghua University, Beijing 100084, China*

[5]*Frontier Science Center for Quantum Information, Beijing 100084, China*

(Received 3 March 2024; accepted 16 May 2024; published 4 June 2024)

Chiral magnetic states in two-dimensional (2D) layered noncentrosymmetric magnets, which are promising advanced spintronic materials, are usually attributed to Dzyaloshinskii–Moriya interactions (DMIs). However, the role of underlying higher-order spin couplings in determining the properties of chiral spin textures has been much less studied. In this work, taking the lithium-decorated monolayer $CrTe_2$ (monolayer $LiCrTe_2$) as an example, we develop a first-principles-based comprehensive spin model constructed by using the symmetry-adapted cluster expansion method. Based on this spin model, we identify the ground state of monolayer $LiCrTe_2$ as a chiral spin spiral state, which can further assemble macroscopic chiral labyrinth domains under zero-field conditions as well as evolve into skyrmions under a finite magnetic field. Moreover, higher-order biquadratic and three-site interactions are identified to be responsible for modulating both the size and the field stability of the spin spiral state. Our study sheds light on complex magnetic couplings in 2D magnets.

DOI: 10.1103/PhysRevB.109.214405

I. INTRODUCTION

Novel chiral spin textures, such as chiral spin spirals (SSs) [1–3] and magnetic skyrmions [4–6], have attracted much attention because they are fertile ground for both emergent magnetoelectric phenomenon explorations [7–10] and advanced spintronic device applications [11–13]. The formation and basic characteristics (i.e., type, morphology, and stability) [14–22] of these chiral spin textures are usually correlated with the asymmetric Dzyaloshinskii-Moriya interaction (DMI) [23–25], which favors a noncollinear spin arrangement. According to Moriya's rule [24], the key to inducing DMI is breaking the centrosymmetry of a system, which can be easily realized in two-dimensional (2D) magnetic materials [26–29]. To date, many strategies for eliminating centrosymmetry in 2D magnetic systems have been theoretically and experimentally considered [29–41].

In addition to DMI, other spin interactions, such as exchange frustration [42–44], magnetic anisotropy [30,45], and Kitaev interactions [30,46], can also have nontrivial effects on the basic properties of chiral spin configurations. Nevertheless, these spin couplings are all limited in the range of second-order interactions. Recently, higher-order spin interactions [47–72] were predicted to exist in some realistic magnetic systems. Interestingly, higher-order interactions were proposed to play unique roles in the morphology and stability of chiral spin textures [49,50,73–75]. One may be curious about whether any higher-order interactions exist in 2D magnets that could significantly influence the emergence of chiral spin textures. If such higher-order interactions exist, what do they look like? How do these higher-order interactions affect the fundamental characteristics of chiral spin structures? To answer these questions, a model system is required.

A suitable system for addressing our concerns above is Li-decorated monolayer $CrTe_2$ (monolayer $LiCrTe_2$). When exfoliated from its bulk form [76,77], monolayer $LiCrTe_2$ is predicted to be energetically and dynamically stable [78], with a significantly high ferromagnetic (FM) transition temperature of approximately 200 K. Importantly, as Li ions are located on one side of $CrTe_2$, the centrosymmetry of the host system is disrupted, which potentially gives rise to a strong DMI. Although previous work theoretically predicted DMI-induced chiral magnetic structures in monolayer $LiCrTe_2$ [79], the effect of underlying higher-order spin interactions on the fundamental characteristics of chiral spin textures remains unclear.

In this work, we reveal which and how higher-order interactions affect the chiral magnetic states of monolayer $LiCrTe_2$. Based on a newly developed symmetry-adapted cluster expansion (SACE) method, we construct a first-principles-based effective spin Hamiltonian. This Hamiltonian not only contains the commonly considered single-ion anisotropy (SIA) and two-body couplings, such as Heisenberg interaction and DMI, but also accommodates symmetry-allowed higher-order spin couplings, which are beyond the framework of widely used second-order spin models. The

*csxu@fudan.edu.cn

resulting effective Hamiltonian predicts Néel-like ferromagnetic SSs as the magnetic ground state of monolayer $LiCrTe_2$. Among the higher-order spin interactions, biquadratic interactions and three-site interactions are identified to have nontrivial effects on the size and stability of SSs. Further, Monte Carlo (MC) simulations demonstrate the emergence of metastable Néel-type skyrmions when considering an external magnetic field.

II. METHODS

A. Computational workflow

Our study proceeds through a systematic four-step process: Initially, we utilize the SACE method to generate all symmetry-allowed spin invariants based on the crystal structure of monolayer $LiCrTe_2$. Subsequently, employing density functional theory (DFT), we compute the energies of various randomly generated spin configurations. In the next stage, we employ a machine learning approach to discern the dominant terms from the myriad possible invariants, thereby effectively reducing their number by fitting the parameters of the spin Hamiltonian. Finally, employing the derived Hamiltonian, we conduct Monte Carlo simulations, followed by a comprehensive analysis. Detailed descriptions of each step are provided below.

B. Spin Hamiltonian from the symmetry-adapted cluster expansion method

The general form of the spin Hamiltonian is written as

$$H = H_0 + \sum_{\mathrm{N}} H_{\mathrm{N}}^{\mathrm{spin}}, \tag{1}$$

where H_0 refers to the nonmagnetic part and $H_{\mathrm{N}}^{\mathrm{spin}}$ indicates the Nth-order spin interaction terms. For example, the dominant second-order and fourth-order terms can be expressed as

$$\begin{aligned} H_{\text{2-order}}^{\mathrm{spin}} &= \sum_{\langle i,j\rangle} \sum_{\alpha,\beta} a_{ij}^{\alpha\beta} S_{i\alpha} S_{j\beta}, \\ H_{\text{4-order}}^{\mathrm{spin}} &= \sum_{\langle i,j,k,l\rangle} \sum_{\alpha,\beta,\gamma,\delta} a_{ijkl}^{\alpha\beta\gamma\delta} S_{i\alpha} S_{j\beta} S_{k\gamma} S_{l\delta}. \end{aligned} \tag{2}$$

Here, the summation encompasses all potential spin components. The index $\langle \cdots \rangle$ refers to an M-body atomic cluster comprising magnetic atoms denoted as i, j, k, and l. The indices α, β, γ, and δ denote spin components. For simplicity, the spins are normalized to $S = 1$ in this study. Considering time-reversal symmetry, only even-order terms are incorporated into this cluster-expansion Hamiltonian. Additionally, to balance accuracy and simplicity, higher-order terms in our model are truncated at the fourth order. Moreover, by regulating the cutoff distance between ions, our model considers only eight dominant clusters, encompassing a single-ion cluster, two-body clusters up to third-nearest neighbors, two three-body clusters, and two four-body clusters (refer to Fig. S4 in the Supplemental Material (SM) [80]).

By further applying crystal symmetries, Eq. (2) can be rewritten as

$$\begin{aligned} H_{\text{2-order}}^{\mathrm{spin}} &= \sum_{n} L_n \sum_{m} a_{nm} S_{i_m\alpha_m} S_{j_m\beta_m}, \\ H_{\text{4-order}}^{\mathrm{spin}} &= \sum_{n} K_n \sum_{m} a_{nm} S_{i_m\alpha_m} S_{j_m\beta_m} S_{k_m\gamma_m} S_{l_m\delta_m}, \end{aligned} \tag{3}$$

where n denotes each isolated invariant, with the summation conducted over m to aggregate all terms within each invariant. It is evident that leveraging crystal symmetries significantly diminishes the number of terms, retaining only those permitted by symmetry. Consequently, this SACE Hamiltonian can theoretically encompass all permissible many-body and higher-order interactions, a scope beyond the confines of a second-order spin Hamiltonian framework.

This section provides technical insights into spin invariant generation using the SACE method. To enhance computational efficiency and model accuracy, it is imperative to truncate three key parameters: the number of interaction orders, denoted as N; the number of sites M encompassing spin interactions; and the maximum interaction distance d_M. Here, d_M is defined such that the interaction distance between any two sites among the M atoms is shorter than d_M. In this study, meticulous testing led to the adoption of $N = 4$, $M = 4$, $d_2 = 9.0$ Å, $d_3 = 6.9$ Å, and $d_4 = 7.9$ Å, ensuring comprehensive representation of dominant interaction patterns within the model while maintaining manageable computational costs.

C. DFT calculations

Having obtained the form of the spin model, we then calculated the energies of various spin configurations with DFT. The energies of spin configurations were used for fitting the spin model. We performed DFT calculations implemented in the Vienna Ab initio Simulation Package (VASP) with the projector augmented wave method. In our computational treatment, the generalized gradient approximation with the Perdew-Burke-Ernzerhof functional was used [81]. During the structural optimization, we fully relaxed both the atomic positions and the lattice constants of the system until the residual Hellmann-Feynman force per atom was less than 0.001 eV/Å. Meanwhile, the electronic convergence criterion was chosen to be 10^{-6}eV. To treat the on-site Coulomb correlation effect of the Cr $3d$ orbitals, we set U and J values to be 3.0 and 0.6 eV, respectively, as in a previous study [82]. Other values of U and J were also tested and do not qualitatively affect our fitted spin model and the predicted magnetic ground state (see Table S3 in the SM [80]). A vacuum region of 20 Å along the out-of-plane direction eliminated interaction between the periodic images. The van der Waals dispersion correction included in the Grimme's semiempricial D3 schema was considered to accurately describe the structural properties [83]. Regarding a unit cell, the cutoff energy of the plane wave was set to 600 eV, with a $15\times15\times1$ Γ-centered k-point mesh sampled in the Brillouin zone. After structural relaxation, the final lattice constant of monolayer $LiCrTe_2$ we obtained is $a = b = 4.06$ Å. To extract the energies of random spin configurations, a $5\times5\times1$ supercell was adopted. In this case, we carefully tested and reset the plane wave cutoff energy to 400 eV, and a Γ-centered k-point mesh of $4\times4\times1$ was

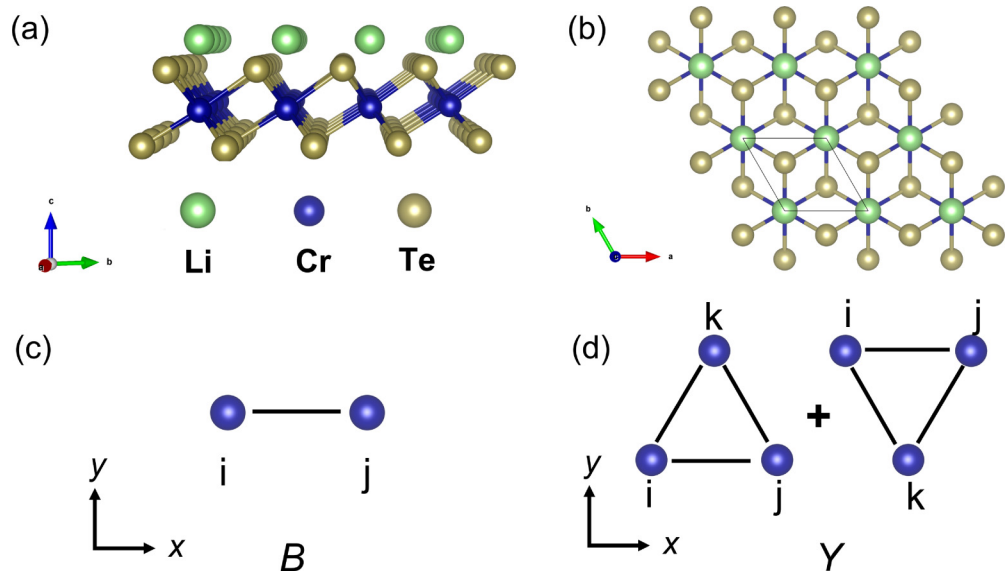

FIG. 1. Crystal structure of monolayer $LiCrTe_2$. (a) Side view of monolayer $LiCrTe_2$. (b) Top view of monolayer $LiCrTe_2$. The parallelogram shows the in-plane unit cell. The atomic clusters involved in (c) the biquadratic interaction and (d) three-site interactions.

adopted, so that the accuracy could be maintained with less computational cost during the supercell calculations. Other choices of supercells were also tested and did not largely affect our fitted spin model (see Table S2 in the SM [80]). During the calculations, the directions of the spins were constrained, while their magnitudes were fully relaxed. In order to fix the spin directions, we set LAMBDA = 10 in VASP, so that the spin would naturally locate near the initial configurations by minimizing the penalty energies. After DFT calculations, we deducted the penalty energy (<0.05 meV/Cr) from the corresponding total DFT energies before fitting the model.

D. Fitting the model with a machine learning approach

The spin configurations and their DFT-calculated energies are used to fit the spin model, so that we can obtain the values of L_n and K_n, as well as E_0 of H_0. To better describe the fitting, we rewrite Eqs. (1)–(3) as

$$E_n = E_0 + \sum_m Y_m C_{n,m}. \tag{4}$$

where E_n is the DFT total energy of the nth spin configuration and $C_{n,m}$ are coefficients corresponding to the mth invariants. The fitting was performed with a machine learning method for constructing a Hamiltonian (MLMCH) as implemented in PASP [84]. Details of this fitting method are given in Refs. [85,86]. This MLMCH method was already used to study various magnetic systems [48,49,87].

In this study, the initial model was developed up to the four-body and fourth-order spin interactions, with distant neighbors extending up to the third-nearest neighbors, while fully considering the spin-orbit coupling (SOC) effect. Subsequently, we conducted energy calculations for 575 random spin structures via DFT. Notably, within these 575 datasets, the training set comprised 444 sets of data, while the testing set comprised 131 sets. Leveraging the energies of these calculated spin structures, we repeated the fit and refined the spin model within the MLMCH framework, ultimately achieving a model with minimal spin interaction terms and optimal numerical performance. For further details, refer to the Supplemental Material [80].

E. Monte Carlo simulations

We carried out parallel tempering Monte Carlo (PTMC) simulations [88] using the fitted Hamiltonian (1)–(3). Based on the unit cell geometry (see Fig. 1), different sizes and shapes of supercells are adopted in our study. To be specific, the $40\times20\times1$ supercell (containing 1600 Cr ions) is used in Fig. 2, while a smaller $30\times15\times1$ supercell (containing 900 Cr ions) is used in Figs. 3 and 4. Both supercells are based on the rectangular cell defined by $\mathbf{a}' = \mathbf{a}$, $\mathbf{b}' = \mathbf{a} + 2\mathbf{b}$, and $\mathbf{c}' = \mathbf{c}$, where $\mathbf{a}$, $\mathbf{b}$, and $\mathbf{c}$ are lattice vectors of the original parallelogram unit cell. During PTMC simulations, the initial magnetic configuration is randomly generated, and 120 000 MC steps are performed for each temperature. To be specific, we set 400 replica exchange steps and 300 MC steps between every two replica exchange steps. The temperature is gradually cooled down from 315 K to the investigated lowest temperature, i.e., 2 K. To further optimize the spin configuration after the MC simulations, a Clebsch-Gordan (CG) method [89] is applied so that the direction of each spin will rotate before the forces on each spin minimize. In this case, the obtained magnetic state is located at its energy minimum. The energy convergence criterion of this CG algorithm is set to be 10^{-6} eV.

III. RESULTS AND DISCUSSION

A. The effective model of monolayer $LiCrTe_2$

The crystal structure of monolayer $LiCrTe_2$ is shown in Figs. 1(a) and 1(b). The Cr atoms form a triangular lattice, and the nearest Cr-Cr distance is evaluated to be 4.06 Å. It can be clearly seen that each Cr atom is surrounded by a Te octahedron; thus, the resulting octahedron crystal field

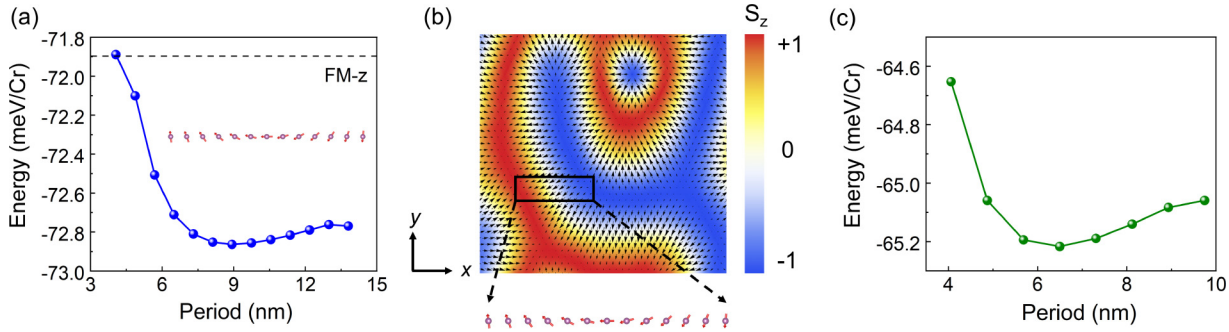

FIG. 2. Magnetic properties of monolayer $LiCrTe_2$. (a) The energy of the spin spiral as a function of its period. The magnetic configuration with the lowest energy has a period of 8.93 nm. The spin spirals are illustrated. (b) Néel-like labyrinth domains. The side view of the selected spin spirals outlined with dashed lines is shown. (c) The energy of the spin spiral as a function of its period but with the higher-order interactions turned off. The magnetic configuration with the lowest energy has a period of 6.50 nm.

splits the $3d$ orbital of the Cr atoms into threefold degenerate t_{2g} levels and twofold degenerate e_g levels. After the local trigonal distortion of the octahedra is considered, the threefold degenerate t_{2g} levels will further split into twofold degenerate e'_g levels and an a_{1g} singlet. By locating a layer of Li atoms on top of monolayer $CrTe_2$, the inversion symmetry of the system is broken, and the overall point group symmetry belongs to C_{3v}. Furthermore, the valence state of Cr changes from Cr^{4+} in pristine monolayer $CrTe_2$ to Cr^{3+} in Li-decorated monolayer $CrTe_2$. In the latter case, the spin-up channel of the Cr $3d$ orbital is occupied by three electrons, while the spin-down channel is empty. This electronic distribution results in a total spin magnetic moment of $S = 3/2$ for each Cr^{3+} ion.

To study the magnetic properties of monolayer $LiCrTe_2$, it is necessary to construct a spin Hamiltonian, which involves all the dominant magnetic interactions. After we construct the spin model using the SACE method [49,85–87] and fit the spin Hamiltonian with the MLMCH approach [48,85], the final spin model reads

$$H = H_{2-\text{order}} + H_{4-\text{order}}, \tag{5}$$

where $H_{2-\text{order}}$ and $H_{4-\text{order}}$ represent the second-order and fourth-order spin interaction terms, respectively. After the important terms are collected, $H_{2-\text{order}}$ is found to be expressed as follows:

$$H_{2-\text{order}} = \sum_{\langle i,j\rangle_1} \left\{ J_1 \mathbf{S}_i \cdot \mathbf{S}_j + K S_i^{\gamma} S_j^{\gamma} + \mathbf{D}_{ij} \cdot (\mathbf{S}_i \times \mathbf{S}_j) \right\} + \sum_{\langle i,j\rangle_2} J_2 \mathbf{S}_i \cdot \mathbf{S}_j + \sum_{\langle i,j\rangle_3} J_3 \mathbf{S}_i \cdot \mathbf{S}_j + \sum_i A_{zz} (S_{iz})^2, \tag{6}$$

where $\langle i, j\rangle_n$ $(n = 1, 2, 3)$ denotes the nth-nearest-neighbor spin pairs. S_γ is the γ component of the spin vector in a local $\{\alpha\beta\gamma\}$ basis (see Fig. S2 in the SM [80]). J_i $(i = 1, 2, 3)$ denotes the isotropic Heisenberg exchange interactions, K denotes the bond-dependent Kitaev interaction, A_{zz} denotes the SIA, and $\mathbf{D}_{ij}$ is the DMI. Because of the C_{3v} symmetry of our system and based on Moriya's rule, $\mathbf{D}_{ij}$ can be further expressed as $d_{//}(\hat{\mathbf{u}}_{ij} \times \hat{\mathbf{z}}) + d_z \hat{\mathbf{z}}$, where $\hat{\mathbf{u}}_{ij}$ connects two first-nearest-neighbor (1NN) Cr atoms, while $d_{//}$ and d_z are the in-plane and out-of-plane components of $\mathbf{D}_{ij}$, respectively.

As shown in Table I, the 1NN isotropic Heisenberg exchange yields strong FM coupling with $J_1 = -25.53$ meV, and the second-nearest-neighbor Heisenberg coupling strength $J_2 = -0.43$ meV is rather weak. However, $J_3 = 3.95$ meV indicates that the third-nearest-neighbor Heisenberg coupling favors antiferromagnetic (AFM) interactions. These two types of interactions compete with each other and give rise to exchange frustration. Moreover, a sizable DMI of $D = |\mathbf{D}_{ij}| = 5.15$ meV, with $d_{//} = -4.74$ meV and $d_z = 2.01$ meV, is predicted. The resulting $|D/J_1|$ ratio of 0.21, which is quite strong if we recall the typical value of 0.1–0.2 in skyrmionic systems, favors the emergence of chiral spin textures in our system.

Now, let us turn to the higher-order terms $H_{4-\text{order}}$. The $H_{4-\text{order}}$ terms are determined to be

$$H_{4-\text{order}} = \sum_{\langle i,j\rangle_1} B(\mathbf{S}_i \cdot \mathbf{S}_j)^2 + \sum_{\langle i,j,k\rangle} Y\{(\mathbf{S}_i \cdot \mathbf{S}_j)(\mathbf{S}_j \cdot \mathbf{S}_k) + (\mathbf{S}_j \cdot \mathbf{S}_k)(\mathbf{S}_k \cdot \mathbf{S}_i) + (\mathbf{S}_k \cdot \mathbf{S}_i)(\mathbf{S}_i \cdot \mathbf{S}_j)\} + H_{4-\text{sites}}, \tag{7}$$

where $\langle i, j, k\rangle$ denotes the nearest-neighbor three-site clusters [see Fig. 1(d)]. B denotes biquadratic interaction, and Y denotes isotropic three-site interaction. As shown in Table I, a strong biquadratic interaction $B = -1.96$ meV and a smaller, but non-neglectable, three-site interaction $Y = -0.35$ meV are predicted. The remaining four-site interactions $H_{4-\text{sites}}$, whose full expression can be found in Table S4 in the SM [80], all have negligible magnitudes and are thus not included here.

TABLE I. Magnetic parameters with significant values. For simplification, we normalized the spins to $S = 1$ in this work. The energy unit is meV. One can refer to Eqs. (6) and (7) for the exact forms of interactions and see details in Sec. C, Fig. S4, and Table S4 in the SM [80].

A_{zz}	J_1	K	$d_{//}$	d_z	J_2	J_3	B	Y
0.05	−25.53	2.30	−4.74	2.01	−0.43	3.95	−1.96	−0.35

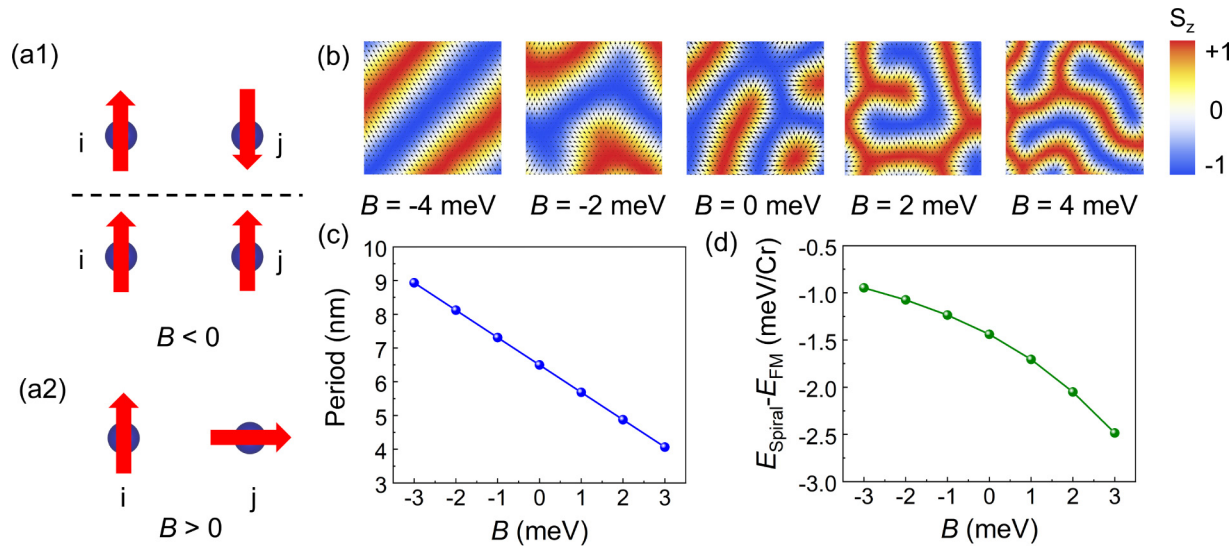

FIG. 3. Role of biquadratic interactions B in monolayer $LiCrTe_2$. (a) The magnetic ground state on a single two-site cluster when only the biquadratic term is turned on. (b) The macroscopic magnetic textures, (c) the lowest-energy period of the SS state, and (d) the energy difference between the SS state and the FM_z state with distinct magnitudes of biquadratic interactions are also shown. Note that in this case, the second-order interactions are all turned on, while higher-order interactions other than B are all turned off.

To validate the reliability of this model, we compare the energies of different spin configurations predicted by this model with corresponding energies achieved from DFT calculations (see Fig. S3 in the SM [80]) and find that the fitting error is as small as 0.21 meV/Cr. This means that the results predicted from our spin model perfectly match those from DFT calculations. By further including the SOC effect on higher-order interactions, the fitting error would slightly decrease to 0.18 meV/Cr, yet the interaction forms would be complicated and bring a huge computational cost. Thus, the SOC effect on higher-order couplings, which deserves future investigation, is excluded in our study.

B. Chiral magnetic state: The effects of DMI and fourth-order interactions

Based on the aforementioned spin Hamiltonian, MC simulations were carried out to explore the low-energy spin textures of monolayer $LiCrTe_2$. The magnetic ground state is identified as a Néel-type SS. By further performing MC simulations on a large supercell, one can see that metastable wormlike chiral labyrinth domains (LDs) with local topological defects emerge, as shown in Fig. 2(b). These metastable LD states are assembled by the aforementioned SSs. Meanwhile, one can identify the period of the ground state SS state as 8.93 nm based on the energy of the SS as a function of its period [see Fig. 2(a)]. In the following text, we denote this lowest-energy SS state obtained from the spin model with higher-order interactions as the SS_1 state. This SS_1 state has a lower energy of -0.97 meV/Cr with respect to the out-of-plane FM (FM_z) state.

To understand the microscopic origin of the SS_1 state, we decompose the energy difference between the SS_1 and FM_z states into interaction terms (see Table S1 in the SM [80]). We can see that the largest energy gain of the SS_1 state with respect to the FM_z state is contributed by the in-plane component of the DMI $d_{//}$, which is responsible for the spin whirling in the x-z plane. Notably, the SS_1 state would collapse into the FM_z state without this $d_{//}$ term. This fact demonstrates that $d_{//}$ plays an indispensable role in the formation of the SS state rather than the collinear FM state. Moreover, $d_{//}$ was also used to choose the chirality of the SS state. To illustrate this, we artificially construct a SS state which has the same period as the SS_1 state but opposite chirality (denoted as SS_1^{OC}). By decomposing the energy difference between the SS_1 state and the SS_1^{OC} state (see Table S1 in the SM [80]), we find that the energy difference is contributed only by $d_{//}$. Furthermore, if we run MC simulations with the value of $d_{//}$ being inverted, a SS with opposite chirality will emerge. From the above results, we thus conclude that it is $d_{//}$ which plays the decisive role in the formation of the SS ground state with certain chirality. Notably, besides $d_{//}$, the AFM J_3, which competes with FM J_1, is also identified to contribute to the energy gain of the SS_1 state with respect to the FM_z state. This is in line with the fact that exchange frustration between FM 1NN interaction and far-neighbor AFM interactions would help stabilize chiral spin textures [44]. The detailed role of DMI and exchange frustration in the emergence of the spin spiral state can be seen in the SM [80].

Interestingly, all the higher-order spin interactions cost energy to the SS_1 state with respect to the FM_z state. This indicates that higher-order interactions could decrease the stability of the SS state, possibly increasing the sensitivity of the SS state under an external field. To identify the effect of higher-order spin interactions on the formation of SSs, we perform MC simulations with only second-order interactions while the higher-order interactions are all turned off. The resulting magnetic ground state without higher-order interactions is still a Néel-type SS, which is termed the SS_2 state here. This implies that the higher-order interactions considered in our system will not qualitatively alter the morphology of the magnetic ground state. However, based on the energy of a SS

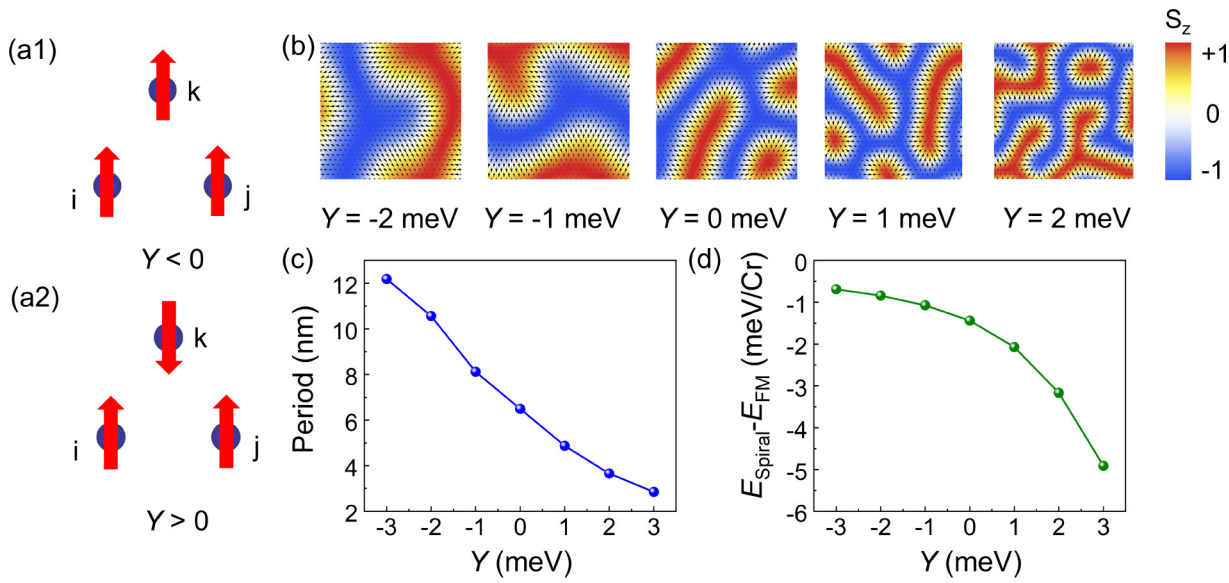

FIG. 4. Role of three-site interactions Y in monolayer $LiCrTe_2$. (a) The magnetic ground state on a single three-site cluster when only the three-site term is turned on. (b) The macroscopic magnetic textures, (c) the lowest-energy period of the SS state, and (d) the energy difference between the SS state and the FM_z state with distinct magnitudes of three-site interactions are also shown. Note that in this case, the second-order interactions are all turned on, while higher-order interactions other than Y are all turned off.

as a function of its period [see Fig. 2(c)], we observe that the period of the SS_2 state is 6.50 nm, which is remarkably shorter than that of SS_1 (8.93 nm). This shows that higher-order interactions alter the period of SSs. To gain quantitative insight, we calculate the energies per Cr atom in the SS_1 and SS_2 states in our initial spin model with higher-order interactions. As shown in Table II, the SS_2 state is 0.15 meV/Cr higher in energy than the SS_1 state. By further decomposing the energy difference between SS_1 and SS_2 into distinct magnetic parameters, we can see that (1) the second-order interactions cause the energy of the SS_1 state to decrease by 0.13 meV/Cr compared with that of the SS_2 state, and (2) the higher-order interactions, which are dominantly contributed by biquadratic interactions and three-site interactions, cause the energy of the SS_1 state to decrease by 0.28 meV/Cr compared with that of the SS_2 state. From the above results, we can thus conclude that by interplaying with second-order interactions, the higher-order interactions would prefer the emergence of a SS state with a longer period.

TABLE II. Total energy and relative energies of SS_1 and SS_2 states, as well as the decomposition of these energies for some selected critical spin interactions. Note that "second order" ("fourth order") means the sum of energy contributions from all second-order (fourth-order) spin interactions. The energy contribution of higher-order interactions is shown separately. B and Y indicate the energy contributions from biquadratic and three-site interactions. "Four sites" means the sum of energy contributions from all four-site spin interactions (No. 13, No. 14, and No. 15 in Table S4 [80]). The full energy contributions from all spin interactions are listed in Table S1 in the Supplemental Material [80]. The energy unit is meV. The value of S is set to be 1.

Coefficient	SS_1	SS_2	$SS_1 - SS_2$
Total	−72.86	−72.71	−0.15
Second order	−65.11	−65.24	0.13
Fourth order	−7.75	−7.47	−0.28
B	−5.63	−5.43	−0.20
Y	−1.99	−1.92	−0.07
Four sites	−0.13	−0.12	−0.01

Now, we investigate exactly how biquadratic interactions B and three-site interactions Y give rise to the SS configuration with a longer period. First, we focus on the effect of B. By having B act on only one nearest-neighbor two-site cluster, we find that when $B < 0$, the nearest-neighbor spins favor a collinear arrangement (up-up or up-down), as shown in Fig. 3(a1). Such a negative B might suppress the frustration and give rise to a more collinear magnetic state. In contrast, when $B > 0$, the nearest-neighbor spins favor a perpendicular arrangement, as shown in Fig. 3(a2), which is similar to the situation predicted only by the DMI. Such a positive B could compete with J_1 and thus lead to noncollinear magnetic textures in the system.

To go further, we attempt to determine how B affects macroscopic spin textures. To that end, we run MC simulations on large supercells with distinct values of B, during which the second-order interactions are maintained. Meanwhile, the other higher-order interactions are all turned off so that we can focus on the effect of B. As shown in Fig. 3(b), by increasing B from negative to positive values, the macroscopic LDs, which are assembled by SSs, become thinner. To gain quantitative insight, we obtain the lowest-energy SSs for distinct values of B, and the predicted period of SSs as a function of B is shown in Fig. 3(c). When the value of B increases from negative to positive, the period of the SSs decreases, which corresponds to the thinner and thinner LDs shown in Fig. 3(b). Moreover, the energy difference between the FM_z state and the SS state as a function of the B value is shown in Fig. 3(d). Clearly, by enhancing B from negative

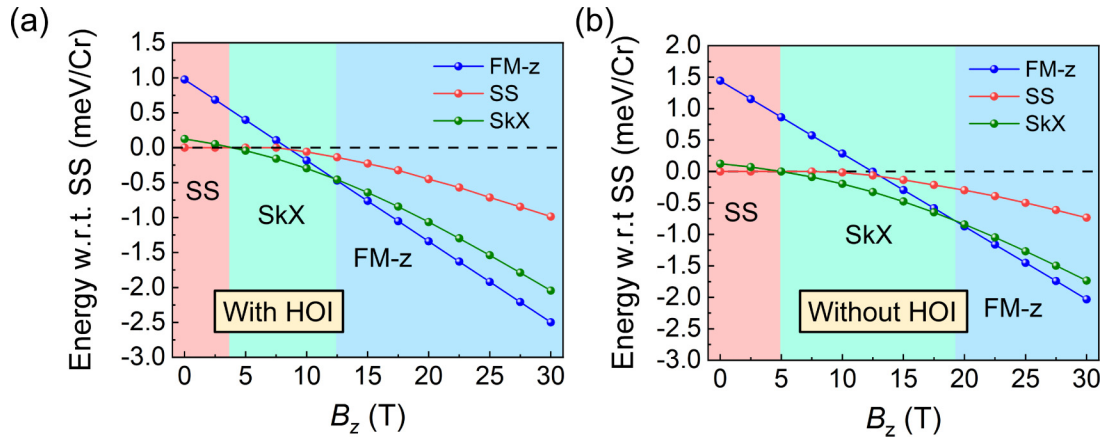

FIG. 5. Low-temperature phase diagram of monolayer $LiCrTe_2$ obtained by (a) including and (b) excluding higher-order interactions. Note that the energies are shown with respect to the zero-field spin spiral state (black dashed line). Here "HOI" means higher-order interactions.

to positive, the energy of the SS becomes much lower than that of the FM_z state, which indicates that SSs are more stable with positive B. Combining the results above with the fact that $B = -1.96$ meV/Cr in our initial model, we can conclude that such a negative B in our system could not only enlarge the period of the SSs but also make the SSs more energetically unstable and thus increase the tunability of SSs under external stimulations.

Next, we clarify the effects of Y. Like in the case of B above, we apply Y to only one nearest-neighbor three-site cluster to investigate the preferred magnetic ground state caused by Y. As shown in Fig. 4(a1), when $Y < 0$, a ferromagnetic state is preferred for the three-site cluster. In this case, the negative Y could enhance the effect of FM Heisenberg interactions J_1 acting on nearest-neighboring spins; thus, collinear magnetic textures with less frustration are favored. In contrast, as shown in Fig. 4(a2), a two-up-one-down AFM spin configuration is favored when $Y > 0$ on the three-site cluster. In this case, the positive Y could compete with FM J_1, and the parallel alignment would be weakened, which benefits the occurrence of noncollinear spin textures.

We also perform MC simulations on a supercell with distinct Y values to examine the effect of Y on the macroscopic spin textures. Like in the case of B, during our MC simulations, the other higher-order interactions are all turned off, and the second-order interactions are maintained. This treatment can effectively show the effect of Y and avoid the influence of other higher-order interactions. As shown in Fig. 4(b), by varying Y from negative to positive values, the macroscopic LDs, which are assembled by a Néel-type SS, become thinner. To gain quantitative insight, we construct the lowest-energy SSs under distinct values of Y and show the period of SSs as a function of Y in Fig. 4(c). By changing the value of Y from negative to positive, the period of the SSs decreases, which qualitatively fits with the thinner LDs shown in Fig. 4(b). The energy difference between the FM_z state and the SS state is also calculated as a function of Y, as shown in Fig. 4(d). Strikingly, by changing Y from negative to positive values, the SS monotonically lowers its energy and thus becomes much more stable than the FM_z state. Recalling that $Y = -0.35$ meV/Cr, which is a negative value, in our initial model, it is thus clear that such negative Y in our system could increase the thickness of the SSs and the metastable LDs. Moreover, the stability of SSs with respect to the FM_z state is suppressed by a positive Y, which makes the SSs and the assembled macroscopic LDs more tunable under external fields.

C. Effect of external field on magnetic states

Since chiral spin textures on a FM background are commonly sensitive to an external magnetic field, the evolution of magnetic states with a magnetic field in our system is naturally considered. To this end, we construct SSs and skyrmion lattices (SkX) with the energetically most favorable sizes and densities. Then, we perform MC simulations with distinct external magnetic fields along the z direction (denoted as B_z) at a low temperature of 2 K so that the spin structures relax to reach their local equilibrium states. The resulting low-temperature phase diagrams, which show the energies of relaxed SSs, SkX, and FM_z states under distinct B_z, are given in Fig. 5(a). The SS state has the lowest energy without an external magnetic field. However, at a certain critical field value of approximately 3 T, SkX is energetically more favorable than the SS state. For a larger critical value of approximately 12.5 T, SkX is suppressed, and the system prefers the FM_z state.

As previously noted, higher-order interactions decrease the energy difference between FM_z and the SS state, which might affect the stability of chiral spin textures under a magnetic field. Here, we provide quantitative insight into this phenomenon by calculating a low-temperature phase diagram without the inclusion of any higher-order interactions. As shown in Fig. 5(b), the magnetic phase transition under B_z (the SS is evolve into SkX and then into FM_z) is similar to that in the presence of higher-order interactions. However, one can still find two qualitative aspects: (1) the value of the critical field for the SS to transform into the SkX increases from approximately 3.5 to approximately 5 T, which means that the SS would be more robust if the effect of higher-order interactions is excluded; (2) the value of the critical field for the SkX to transform to FM_z increases from

approximately 12.5 to approximately 19 T, which implies that a larger magnetic field is needed to fully suppress the chiral magnetic textures without the inclusion of higher-order interactions. These results suggest that the higher-order interactions in our system increase the sensitivity of the chiral magnetic textures to the external field, which will be beneficial for realizing field-sensitive spintronics devices in the future.

IV. CONCLUSIONS

In conclusion, by using the symmetry-adapted cluster expansion method, we constructed a first-principles-based spin model for monolayer $LiCrTe_2$, which predicted a chiral spin spiral state as the ground state. Moreover, this model revealed the existence of higher-order interactions in the system, which expand the size of spin spirals and increase the field tunability of chiral spin textures under external magnetic fields. Our work not only provides comprehensive knowledge of the complex magnetic interactions in 2D magnetic systems but also sheds lights on field-tunable spintronics devices based on chiral spin textures.

ACKNOWLEDGMENTS

We thank X. Zou and B. Zhang for helpful discussion. C.X. acknowledges financial support from the Ministry of Science and Technology of the People's Republic of China (Grant No. 2022YFA1402901), NSFC (Grant No. 12274082), the Shanghai Science and Technology Committee (Grant No. 23ZR1406600), and the open project of the Guangdong Provincial Key Laboratory of Magnetoelectric Physics and Devices (Grant No. 2022B1212010008). W.D. acknowledges financial support from the Basic Science Center Project of NSFC (Grant No. 52388201) and the Beijing Advanced Innovation Center for Future Chip (ICFC).

[1] M. Bode, M. Heide, K. Von Bergmann, P. Ferriani, S. Heinze, G. Bihlmayer, A. Kubetzka, O. Pietzsch, S. Blügel, and R. Wiesendanger, Chiral magnetic order at surfaces driven by inversion asymmetry, Nature (London) **447**, 190 (2007).

[2] J. H. Franken, M. Herps, H. J. Swagten, and B. Koopmans, Tunable chiral spin texture in magnetic domain-walls, Sci. Rep. **4**, 5248 (2014).

[3] K.-S. Ryu, L. Thomas, S.-H. Yang, and S. Parkin, Chiral spin torque at magnetic domain walls, Nat. Nanotechnol. **8**, 527 (2013).

[4] S. Mühlbauer, B. Binz, F. Jonietz, C. Pfleiderer, A. Rosch, A. Neubauer, R. Georgii, and P. Böni, Skyrmion lattice in a chiral magnet, Science **323**, 915 (2009).

[5] X. Yu, Y. Onose, N. Kanazawa, J. H. Park, J. Han, Y. Matsui, N. Nagaosa, and Y. Tokura, Real-space observation of a two-dimensional skyrmion crystal, Nature (London) **465**, 901 (2010).

[6] A. Fert, N. Reyren, and V. Cros, Magnetic skyrmions: Advances in physics and potential applications, Nat. Rev. Mater. **2**, 17031 (2017).

[7] S. Bhowal and N. A. Spaldin, Magnetoelectric classification of skyrmions, Phys. Rev. Lett. **128**, 227204 (2022).

[8] C. Ederer and N. A. Spaldin, Towards a microscopic theory of toroidal moments in bulk periodic crystals, Phys. Rev. B **76**, 214404 (2007).

[9] Y. Li, N. Kanazawa, X. Z. Yu, A. Tsukazaki, M. Kawasaki, M. Ichikawa, X. F. Jin, F. Kagawa, and Y. Tokura, Robust formation of skyrmions and topological Hall effect anomaly in epitaxial thin films of MnSi, Phys. Rev. Lett. **110**, 117202 (2013).

[10] T. Schulz, R. Ritz, A. Bauer, M. Halder, M. Wagner, C. Franz, C. Pfleiderer, K. Everschor, M. Garst, and A. Rosch, Emergent electrodynamics of skyrmions in a chiral magnet, Nat. Phys. **8**, 301 (2012).

[11] S.-H. Yang, R. Naaman, Y. Paltiel, and S. S. Parkin, Chiral spintronics, Nat. Rev. Phys. **3**, 328 (2021).

[12] S. S. Parkin, M. Hayashi, and L. Thomas, Magnetic domain-wall racetrack memory, Science **320**, 190 (2008).

[13] M. Mochizuki and S. Seki, Magnetoelectric resonances and predicted microwave diode effect of the skyrmion crystal in a multiferroic chiral-lattice magnet, Phys. Rev. B **87**, 134403 (2013).

[14] S. Haldar, S. von Malottki, S. Meyer, P. F. Bessarab, and S. Heinze, First-principles prediction of sub-10-nm skyrmions in Pd/Fe bilayers on Rh(111), Phys. Rev. B **98**, 060413(R) (2018).

[15] M. A. Goerzen, S. von Malottki, G. J. Kwiatkowski, P. F. Bessarab, and S. Heinze, Atomistic spin simulations of electric-field-assisted nucleation and annihilation of magnetic skyrmions in Pd/Fe/Ir(111), Phys. Rev. B **105**, 214435 (2022).

[16] D. Li, S. Haldar, and S. Heinze, Strain-driven zero-field near-10 nm skyrmions in two-dimensional van der Waals heterostructures, Nano Lett. **22**, 7706 (2022).

[17] D. Li, S. Haldar, and S. Heinze, Prediction of stable nanoscale skyrmions in monolayer Fe_5GeTe_2, arXiv:2401.18000.

[18] A. S. Varentcova, S. von Malottki, M. N. Potkina, G. Kwiatkowski, S. Heinze, and P. F. Bessarab, Toward room-temperature nanoscale skyrmions in ultrathin films, npj Comput. Mater. **6**, 193 (2020).

[19] Z. He, K. Dou, W. Du, Y. Dai, B. Huang, and Y. Ma, Mixed Bloch-Néel type skyrmions in a two-dimensional lattice, Phys. Rev. B **109**, 024420 (2024).

[20] K. Huang, E. Schwartz, D.-F. Shao, A. A. Kovalev, and E. Y. Tsymbal, Magnetic antiskyrmions in two-dimensional van der Waals magnets engineered by layer stacking, Phys. Rev. B **109**, 024426 (2024).

[21] M. Hoffmann, B. Zimmermann, G. P. Müller, D. Schürhoff, N. S. Kiselev, C. Melcher, and S. Blügel, Antiskyrmions stabilized at interfaces by anisotropic Dzyaloshinskii-Moriya interactions, Nat. Commun. **8**, 308 (2017).

[22] W. Du, K. Dou, Z. He, Y. Dai, B. Huang, and Y. Ma, Bloch-type magnetic skyrmions in two-dimensional lattices, Mater. Horiz. **10**, 5071 (2023).

[23] T. Moriya, New mechanism of anisotropic superexchange interaction, Phys. Rev. Lett. **4**, 228 (1960).

[24] I. Dzyaloshinsky, A thermodynamic theory of "weak" ferromagnetism of antiferromagnetics, J. Phys. Chem. Solids **4**, 241 (1958).

[25] T. Moriya, Anisotropic superexchange interaction and weak ferromagnetism, Phys. Rev. **120**, 91 (1960).

[26] B. Huang *et al.*, Layer-dependent ferromagnetism in a van der Waals crystal down to the monolayer limit, Nature (London) **546**, 270 (2017).

[27] C. Gong *et al.*, Discovery of intrinsic ferromagnetism in two-dimensional van der Waals crystals, Nature (London) **546**, 265 (2017).

[28] Y. Deng *et al.*, Gate-tunable room-temperature ferromagnetism in two-dimensional Fe_3GeTe_2, Nature (London) **563**, 94 (2018).

[29] L. Du, T. Hasan, A. Castellanos-Gomez, G.-B. Liu, Y. Yao, C. N. Lau, and Z. Sun, Engineering symmetry breaking in 2D layered materials, Nat. Rev. Phys. **3**, 193 (2021).

[30] C. Xu, J. Feng, S. Prokhorenko, Y. Nahas, H. Xiang, and L. Bellaiche, Topological spin texture in Janus monolayers of the chromium trihalides $Cr(I, X)_3$, Phys. Rev. B **101**, 060404(R) (2020).

[31] Y. Zhang, C. Xu, P. Chen, Y. Nahas, S. Prokhorenko, and L. Bellaiche, Emergence of skyrmionium in a two-dimensional $CrGe(Te, Se)_3$ Janus monolayer, Phys. Rev. B **102**, 241107(R) (2020).

[32] Y. Hou, F. Xue, L. Qiu, Z. Wang, and R. Wu, Multifunctional two-dimensional van der Waals Janus magnet Cr-based dichalcogenide halides, npj Comput. Mater. **8**, 120 (2022).

[33] C. Huang, J. Guan, Q. Li, F. Wu, P. Jena, and E. Kan, Built-in electric field control of magnetic coupling in van der Waals semiconductors, Phys. Rev. B **103**, L140410 (2021).

[34] J. Liang, Q. Cui, and H. Yang, Electrically switchable Rashba-type Dzyaloshinskii-Moriya interaction and skyrmion in two-dimensional magnetoelectric multiferroics, Phys. Rev. B **102**, 220409(R) (2020).

[35] C. Xu, P. Chen, H. Tan, Y. Yang, H. Xiang, and L. Bellaiche, Electric-field switching of magnetic topological charge in type-I multiferroics, Phys. Rev. Lett. **125**, 037203 (2020).

[36] Q. Tong, F. Liu, J. Xiao, and W. Yao, Skyrmions in the Moiré of van der waals 2D magnets, Nano Lett. **18**, 7194 (2018).

[37] K. Hejazi, Z.-X. Luo, and L. Balents, Heterobilayer Moiré magnets: Moiré skyrmions and commensurate-incommensurate transitions, Phys. Rev. B **104**, L100406 (2021).

[38] S. Chatterjee, N. Bultinck, and M. P. Zaletel, Symmetry breaking and skyrmionic transport in twisted bilayer graphene, Phys. Rev. B **101**, 165141 (2020).

[39] Q. Cui, Y. Zhu, J. Jiang, J. Liang, D. Yu, P. Cui, and H. Yang, Ferroelectrically controlled topological magnetic phase in a Janus-magnet-based multiferroic heterostructure, Phys. Rev. Res. **3**, 043011 (2021).

[40] K. Dou, W. Du, Y. Dai, B. Huang, and Y. Ma, Two-dimensional magnetoelectric multiferroics in a $MnSTe/In_2Se_3$ heterobilayer with ferroelectrically controllable skyrmions, Phys. Rev. B **105**, 205427 (2022).

[41] Y. Wu *et al.*, A van der Waals interface hosting two groups of magnetic skyrmions, Adv. Mater. **34**, 2110583 (2022).

[42] N. Abuawwad, M. dos Santos Dias, H. Abusara, and S. Lounis, Noncollinear magnetism in two-dimensional $CrTe_2$, J. Phys.: Condens. Matter **34**, 454001 (2022).

[43] Y. Hu, X. Chi, X. Li, Y. Liu, and A. Du, Creation and annihilation of skyrmions in the frustrated magnets with competing exchange interactions, Sci. Rep. **7**, 16079 (2017).

[44] S. von Malottki, B. Dupé, P. F. Bessarab, A. Delin, and S. Heinze, Enhanced skyrmion stability due to exchange frustration, Sci. Rep. **7**, 12299 (2017).

[45] Z. Shen, S. Dong, and X. Yao, Manipulation of magnetic topological textures via perpendicular strain and polarization in van der Waals magnetoelectric heterostructures, Phys. Rev. B **108**, L140412 (2023).

[46] D. Amoroso, P. Barone, and S. Picozzi, Spontaneous skyrmionic lattice from anisotropic symmetric exchange in a Ni-halide monolayer, Nat. Commun. **11**, 5784 (2020).

[47] S. Hayami, R. Ozawa, and Y. Motome, Effective bilinear-biquadratic model for noncoplanar ordering in itinerant magnets, Phys. Rev. B **95**, 224424 (2017).

[48] J. Y. Ni, X. Y. Li, D. Amoroso, X. He, J. S. Feng, E. J. Kan, S. Picozzi, and H. J. Xiang, Giant biquadratic exchange in 2D magnets and its role in stabilizing ferromagnetism of $NiCl_2$ monolayers, Phys. Rev. Lett. **127**, 247204 (2021).

[49] C. Xu, X. Li, P. Chen, Y. Zhang, H. Xiang, and L. Bellaiche, Assembling diverse skyrmionic phases in Fe_3GeTe_2 monolayers, Adv. Mater. **34**, 2107779 (2022).

[50] S. Haldar, S. Meyer, A. Kubetzka, and S. Heinze, Distorted $3Q$ state driven by topological-chiral magnetic interactions, Phys. Rev. B **104**, L180404 (2021).

[51] M. Gutzeit, S. Haldar, S. Meyer, and S. Heinze, Trends of higher-order exchange interactions in transition metal trilayers, Phys. Rev. B **104**, 024420 (2021).

[52] M. Hoffmann and S. Blügel, Systematic derivation of realistic spin models for beyond-Heisenberg solids, Phys. Rev. B **101**, 024418 (2020).

[53] S. Mankovsky, S. Polesya, and H. Ebert, Topologically driven three-spin chiral exchange interactions treated from first principles, Phys. Rev. B **104**, 054418 (2021).

[54] S. Brinker, M. dos Santos Dias, and S. Lounis, Prospecting chiral multisite interactions in prototypical magnetic systems, Phys. Rev. Res. **2**, 033240 (2020).

[55] M. dos Santos Dias, S. Brinker, A. Lászlóffy, B. Nyári, S. Blügel, L. Szunyogh, and S. Lounis, Proper and improper chiral magnetic interactions, Phys. Rev. B **103**, L140408 (2021).

[56] S. Lounis, Multiple-scattering approach for multi-spin chiral magnetic interactions: Application to the one- and two-dimensional Rashba electron gas, New J. Phys. **22**, 103003 (2020).

[57] S. Brinker, M. d. S. Dias, and S. Lounis, The chiral biquadratic pair interaction, New J. Phys. **21**, 083015 (2019).

[58] S. Grytsiuk, J.-P. Hanke, M. Hoffmann, J. Bouaziz, O. Gomonay, G. Bihlmayer, S. Lounis, Y. Mokrousov, and S. Blügel, Topological–chiral magnetic interactions driven by emergent orbital magnetism, Nat. Commun. **11**, 511 (2020).

[59] E. Simon, A. Donges, L. Szunyogh, and U. Nowak, Noncollinear antiferromagnetic states in Ru-based Heusler compounds induced by biquadratic coupling, Phys. Rev. Mater. **4**, 084408 (2020).

[60] N. Romming, H. Pralow, A. Kubetzka, M. Hoffmann, S. von Malottki, S. Meyer, B. Dupé, R. Wiesendanger, K. von Bergmann, and S. Heinze, Competition of Dzyaloshinskii-Moriya and higher-order exchange interactions in Rh/Fe atomic bilayers on Ir(111), Phys. Rev. Lett. **120**, 207201 (2018).

[61] A. Krönlein, M. Schmitt, M. Hoffmann, J. Kemmer, N. Seubert, M. Vogt, J. Küspert, M. Böhme, B. Alonazi, J. Kügel, H. A. Albrithen, M. Bode, G. Bihlmayer, and S. Blügel, Magnetic ground state stabilized by three-site interactions: Fe/Rh(111), Phys. Rev. Lett. **120**, 207202 (2018).

[62] J. Spethmann, S. Meyer, K. von Bergmann, R. Wiesendanger, S. Heinze, and A. Kubetzka, Discovery of magnetic single- and triple-**q** states in Mn/Re(0001), Phys. Rev. Lett. **124**, 227203 (2020).

[63] D. Pasquier and O. V. Yazyev, *Ab initio* theory of magnetism in two-dimensional 1*T*-TaS_2, Phys. Rev. B **105**, L081106 (2022).

[64] H.-F. Zhu, H.-Y. Cao, Y. Xie, Y.-S. Hou, S. Chen, H. Xiang, and X.-G. Gong, Giant biquadratic interaction-induced magnetic anisotropy in the iron-based superconductor $A_xFe_{2-y}Se_2$, Phys. Rev. B **93**, 024511 (2016).

[65] N. S. Fedorova, C. Ederer, N. A. Spaldin, and A. Scaramucci, Biquadratic and ring exchange interactions in orthorhombic perovskite manganites, Phys. Rev. B **91**, 165122 (2015).

[66] H. Zhu, Y. Gao, Y. Hou, Z. Gui, and L. Huang, Insight into strain and electronic correlation dependent magnetism in monolayer 1T-$CrTe_2$, Phys. Rev. B **108**, 144404 (2023).

[67] A. Kartsev, M. Augustin, R. F. Evans, K. S. Novoselov, and E. J. Santos, Biquadratic exchange interactions in two-dimensional magnets, npj Comput. Mater. **6**, 150 (2020).

[68] J. Wang and Z.-X. Liu, Effect of ring-exchange interactions in the extended Kitaev honeycomb model, Phys. Rev. B **108**, 014437 (2023).

[69] R. Pohle, N. Shannon, and Y. Motome, Spin nematics meet spin liquids: Exotic quantum phases in the spin-1 bilinear-biquadratic model with Kitaev interactions, Phys. Rev. B **107**, L140403 (2023).

[70] K. Majumdar, D. Furton, and G. S. Uhrig, Effects of ring exchange interaction on the Néel phase of two-dimensional, spatially anisotropic, frustrated Heisenberg quantum antiferromagnet, Phys. Rev. B **85**, 144420 (2012).

[71] M. Amirabbasi and P. Kratzer, Orbital and magnetic ordering in single-layer $FePS_3$: A DFT + U study, Phys. Rev. B **107**, 024401 (2023).

[72] A. Razpopov, D. A. Kaib, S. Backes, L. Balents, S. D. Wilson, F. Ferrari, K. Riedl, and R. Valentí, A $j_{\text{eff}} = 1/2$ Kitaev material on the triangular lattice: The case of $NaRuO_2$, npj Quantum Mater. **8**, 36 (2023).

[73] P. Li, D. Yu, J. Liang, Y. Ga, and H. Yang, Topological spin textures in 1*T*-phase Janus magnets: Interplay between Dzyaloshinskii-Moriya interaction, magnetic frustration, and isotropic higher-order interactions, Phys. Rev. B **107**, 054408 (2023).

[74] S. Paul, S. Haldar, S. Von Malottki, and S. Heinze, Role of higher-order exchange interactions for skyrmion stability, Nat. Commun. **11**, 4756 (2020).

[75] S. Paul and S. Heinze, Electric-field driven stability control of skyrmions in an ultrathin transition-metal film, npj Comput. Mater. **8**, 105 (2022).

[76] S. Kobayashi, H. Ueda, C. Michioka, and K. Yoshimura, Competition between the direct exchange interaction and superexchange interaction in layered compounds $LiCrSe_2$, $LiCrTe_2$, and $NaCrTe_2$ with a triangular lattice, Inorg. Chem. **55**, 7407 (2016).

[77] E. Nocerino *et al.*, Nuclear and magnetic spin structure of the antiferromagnetic triangular lattice compound $LiCrSe_2$ investigated by $\mu+$ SR, neutron and x-ray diffraction, Sci. Rep. **12**, 21657 (2022).

[78] W. Xu, S. Ali, Y. Jin, X. Wu, and H. Xu, Intrinsic ferromagnetic semiconductors in two-dimensional alkali-based chromium chalcogenides, ACS Appl. Electron. Mater. **2**, 3853 (2020).

[79] P. Li, Q. Cui, Y. Ga, J. Liang, and H. Yang, Large Dzyaloshinskii-Moriya interaction and field-free topological chiral spin states in two-dimensional alkali-based chromium chalcogenides, Phys. Rev. B **106**, 024419 (2022).

[80] See Supplemental Material at http://link.aps.org/supplemental/10.1103/PhysRevB.109.214405 for more details about the absorption site of Li atoms, a test of the spin models, and more details about the parameters of the spin models, which includes Refs. [57,78,79].

[81] J. P. Perdew, K. Burke, and M. Ernzerhof, Generalized gradient approximation made simple, Phys. Rev. Lett. **77**, 3865 (1996).

[82] L. Wu, L. Zhou, X. Zhou, C. Wang, and W. Ji, In-plane epitaxy-strain-tuning intralayer and interlayer magnetic coupling in $CrSe_2$ and $CrTe_2$ monolayers and bilayers, Phys. Rev. B **106**, L081401 (2022).

[83] S. Grimme, J. Antony, S. Ehrlich, and H. Krieg, A consistent and accurate ab initio parametrization of density functional dispersion correction (DFT + D) for the 94 elements H-Pu, J. Chem. Phys. **132**, 154104 (2010).

[84] F. Lou, X. Li, J. Ji, H. Yu, J. Feng, X. Gong, and H. Xiang, PASP: Property analysis and simulation package for materials, J. Chem. Phys. **154**, 114103 (2021).

[85] X.-Y. Li, F. Lou, X.-G. Gong, and H. Xiang, Constructing realistic effective spin Hamiltonians with machine learning approaches, New J. Phys. **22**, 053036 (2020).

[86] C. Xu, H. Yu, J. Wang, and H. Xiang, First-principles approaches to magnetoelectric multiferroics, Annu. Rev. Condens. Matter Phys. **15**, 85 (2024).

[87] X. Li, C. Xu, B. Liu, X. Li, L. Bellaiche, and H. Xiang, Realistic spin model for multiferroic NiI_2, Phys. Rev. Lett. **131**, 036701 (2023).

[88] K. Hukushima and K. Nemoto, Exchange Monte Carlo method and application to spin glass simulations, J. Phys. Soc. Jpn. **65**, 1604 (1996).

[89] M. R. Hestenes and E. Stiefel, Methods of conjugate gradients for solving linear systems, J. Res. Natl. Bur. Stand. (US) **49**, 409 (1952).